Science of the Total Environment 774 (2021) 145154

Contents lists available at ScienceDirect

Science of the Total Environment

journal homepage: www.elsevier.com/locate/scitotenv

A long-term spatiotemporal analysis of biocrusts across a diverse arid environment: The case of the Israeli-Egyptian sandfield

Klil Noy [a], Noa Ohana-Levi [a,b], Natalya Panov [a], Micha Silver [a], Arnon Karnieli [a,*]

[a] The Remote Sensing Laboratory, French Associates Institute for Agriculture and Biotechnology of Drylands, the Jacob Blaustein Institutes for Desert Research, Ben-Gurion University, Sede Boker Campus, 84990, Israel
[b] Independent researcher, Ashalim, 85512, Israel

HIGHLIGHTS

- Time series of Crust Index (CI), based on remote sensing retrievals, was used.
- Short- and long-term trend analysis was performed over the CI time series.
- The area was partitioned into 3 clusters that represent the spatiotemporal dynamic.
- Biocrust dynamics was found to alter locally due to anthropogenic factors.
- Regionally, biocrusts are affected by long-term precipitation dynamics.

GRAPHICAL ABSTRACT

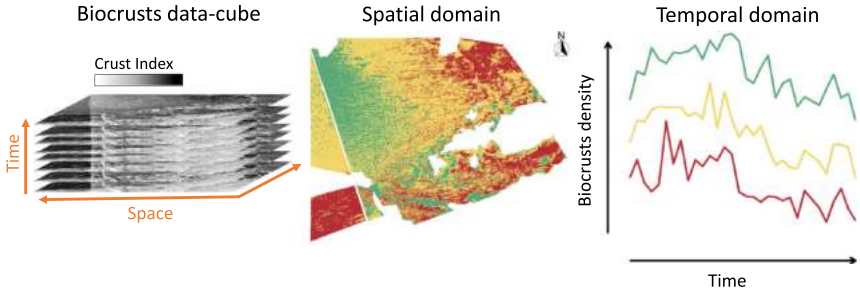

ARTICLE INFO

Article history:
Received 26 November 2020
Received in revised form 5 January 2021
Accepted 8 January 2021
Available online 6 February 2021

Editor: Fernando A.L. Pacheco

Keywords:
Crust Index
Time-series clustering
Long-term trend
Landsat
Remote sensing

ABSTRACT

Spatiotemporal data can be analyzed using spatial, time-series, and machine learning algorithms to extract regional biocrust trends. Analyzing the spatial trends of biocrusts through time, using satellite imagery, may improve the quantification and understanding of their change drivers. The current work strives to develop a unique framework for analyzing spatiotemporal trends of the spectral Crust Index (CI), thus identifying the drivers of the biocrusts' spatial and temporal patterns. To fulfill this goal, CI maps, derived from 31 annual Landsat images, were analyzed by applying advanced statistical and machine learning algorithms. A comprehensive overview of biocrusts' spatiotemporal patterns was achieved using an integrative approach, including a long-term analysis, using the Mann-Kendall (MK) statistical test, and a short-term analysis, using a rolling MK with a window size of five years. Additionally, temporal clustering, using the partition around medoids (PAM) algorithm, was applied to model the spatial multi-annual dynamics of the CI. A Granger Causality test was then applied to quantify the relations between CI dynamics and precipitation. The findings show that 88.7% of pixels experienced a significant negative change, and only 0.5% experienced a significant positive change. A strong association was found in temporal trends among all clusters ($0.67 \le r \le 0.8$), signifying a regional effect due to precipitation levels ($p < 0.05$ for most clusters). The biocrust dynamics were also locally affected by anthropogenic factors ($0.58 > CI > 0.64$ and $0.64 > CI > 0.71$ for strongly and weakly affected regions, respectively). A spatiotemporal analysis of a series of spaceborne images may improve conservation management by evaluating biocrust development in drylands. The suggested framework may also by applied to various disciplines related to quantifying spatial and temporal trends.

1. Introduction

Remote sensing is a commonly used tool for monitoring spatial and temporal phenomena (Jat et al., 2008; Karnieli et al., 2014; Rawat and

* Corresponding author.
E-mail address: karnieli@bgu.ac.il (A. Karnieli).

https://doi.org/10.1016/j.scitotenv.2021.145154

Kumar, 2015). Spatiotemporal data can be analyzed using different procedures, such as spatial and time-series statistics and machine learning algorithms used to define the trends of various types of remote sensing retrievals. Time-series analysis, conducted on a set of images, enables the evaluation of the change within a study area in general, the specific trend of each pixel over the years, and the relative change among pixels (Burrell et al., 2017; Verbesselt et al., 2010). A set of consecutive satellite images with equal temporal intervals constitutes a time series for each pixel. As the abundance of free satellite images continues to accumulate, the volume of available remote sensing data has substantially increased (Zhu et al., 2018). Furthermore, the cost of data storage has decreased considerably, and there is constant advancement and higher efficiency in the management strategies of remotely sensed imagery (Jing and Tian, 2018). In recent years, there has been a great improvement in computing power, enabling the improvement of modeling algorithms and the application of faster, more accurate time series methods (Zhu, 2017).

The choice of the analysis of the temporal dynamics for each pixel in an image depends on the objectives of the study. Various methods have been documented for analyzing temporal dynamics, including the Mann-Kendall test for monotonic trend (Hamed and Ramachandra Rao, 1998; Kendall, 1955; Mann, 1945; Ohana-Levi et al., 2019), change detection (Bruzzone and Prieto, 2000; Bruzzone and Serpico, 1997), Change Vector Analysis (CVA) (Bayarjargal et al., 2006; Karnieli et al., 2014; Zanchetta et al., 2016), Breaks For Additive Seasonal and Trend (BFAST) (Dutrieux et al., 2015; Permatasari et al., 2016; Verbesselt et al., 2010), Residual Trends (RESTREND) (Burrell et al., 2017; Evans and Geerken, 2004; Higginbottom and Symeonakis, 2014), and others. Further use of time-series analysis includes time series forecasting in various fields of research and applications.

Quantification of relative trends among pixels within the study domain enables homogeneous groups of pixels to be clustered together while relying on the time series vector of each pixel (Ohana-Levi et al., 2020). The clusters are determined according to the similarities among the temporal dynamics of the entities (Aghabozorgi et al., 2015). In remote sensing, time series clustering (TSC) algorithms have mainly been applied for defining land-cover types (Petitjean et al., 2012; Zhang et al., 2008; Zhang et al., 2014). Different studies used the TSC of NDVI images to evaluate the dynamics of regions over time (Romani et al., 2011; Viovy, 2000). TSC has also been used successfully to cluster the temporal data of temperature levels across sea (Bograd et al., 2005) and land (Müller-Hansen et al., 2017; Peng et al., 2018).

In the current project, the TSC algorithms are applied to monitoring biocrusts, in a sandy environment across the Israel-Egypt political border. Although the sandfield in the northwestern Negev Desert (Israel) is an extension of the one in northeastern Sinai (Egypt), after the establishment of the State of Israel in 1948, the Negev dunes changed their characteristics, transforming to stabilized dunes, while the Sinai dunes have remained active (Karnieli and Tsoar, 1995). This stabilization process is mainly caused by windblown microorganisms, especially cyanobacteria, together with fine particles (i.e., silt and clay) (Karnieli et al., 1996). Minimal human activity occurs in the Israeli region due to the State of Israel's strict conservation policy and restricted civilian activity in the border vicinity. Conversely, the Egyptian side of the border has experienced anthropogenic pressure due to human activities and overgrazing, resulting in the trampling of the sands and destruction of the fragile crusty topsoil, thus preventing biocrust establishment and enabling dune mobility (Kidron, 2016).

Since the biocrusts have lower reflectance values (albedo) than the exposed sand dunes, earth observation imagery depicts a brightness contrast across the border. The Israeli side appears much darker than the Egyptian side (Tsoar and Karnieli, 1996). The advantage of using satellite imagery lies in generating an extensive temporal range of data that enables spatial and temporal changes to be quantified within a specific scene. Several spectral approaches have been developed to explore the unique spectral reflectance of different types of biocrusts and map biocrusted areas (Chamizo et al., 2012; Chen et al., 2005; Karnieli, 1997; Weber et al., 2008). One of these approaches relies on the Crust Index (CI) that is based on the normalized difference between the red and blue spectral bands (Karnieli, 1997). The CI has been used effectively in different locations worldwide. For example, the CI and the Biological Soil Crust Index (BSCI) were applied with the Random Forest (RF) algorithm to identify and map biocrusts using multispectral optical information in the Mu Us Sandy Land in China (Chen et al., 2019). Studies used the CI to investigate the distribution of microphytes under wet and dry conditions in inner Mongolia (Chen et al., 2020; Fang et al., 2015). Paz-Kagan et al. (2014) used the CI to detect changes in shrubland landscapes in response to drought.

While previous studies focused on monitoring and quantifying the unique contrast around the border (Otterman, 1974; Roskin et al., 2012; Rozenstein et al., 2016; Tsoar and Karnieli, 1996), none focused on the spatial and temporal trends over the years. Investigating the changes in biocrusts, both in time and in space, is essential for understanding ecosystem processes, such as soil stabilization and water cycles, that may respond to climate-change-induced processes in drylands (Panigada et al., 2019; Reed et al., 2016). Quantification of the space-time dynamics of the CI strongly relies on powerful, complex methods and data mining tools. These methods can improve the CI analysis and highlight specific characteristics of spatial trends through time, thus identifying the drivers of change in biocrusts and the spatial and temporal patterns of their effects.

The current work strives to develop a unique framework for analyzing CI spatiotemporal trends based on a time series of Landsat imagery. The suggested approach may assist in detecting the environmental, climatic, and anthropogenic factors causing the spatially diverse long-term trends, their rates, magnitudes, and directions of change. To explore these factors, three objectives were defined: (1) to explore the long-term dynamics of the CI in the study area; (2) to explore the short-term dynamics of the CI in the study area; (3) to partition the study area into different groups based on the similarities in temporal patterns.

The following sections illustrate the methodology that comprises a description of the dataset used in the study. These sections include long- and short-term temporal analyses of the CI, a clustering algorithm applied over the series of CI images, and a quantification of the temporal relationship between the CI and precipitation across the study site. The Results section reports the findings of the analyses mentioned above, followed by their interpretation in the Discussion section. Lastly, a Conclusion section summarizes and clarifies the principal issues raised by this study.

2. Methodology

2.1. Study area

The selected study area is located in the vicinity of the border between northeastern Sinai (Egypt) and the northwestern Negev Desert (Israel), centered at 31.037059°N 34.460345°E (Fig. 1a). The area is composed only of the dunefield, while other land cover types, such as agricultural plots, gravelly valleys, and settlements, are masked out (Fig. 1b). The domain on the Israeli side of the border includes a military training area in the northeast (Fig. 1b). The study area is characterized by an arid climate and a precipitation gradient of mean annual amounts that range from 80 mm in the south to about 200 mm in the north (Tsoar and Møller, 1986; Yair, 1990). The sands originated in the Nile Delta and were transported eastward during the Late Pleistocene and the Holocene eras (Roskin et al., 2011). In the past, the Negev and Sinai sections of the dunefield did not differ in their geomorphological, botanical, topographic, or climatic aspects. However, the agreement between the Ottoman and British empires in 1906 resulted in a separation of the dunefield by a political border. Since the establishment of the State of Israel in

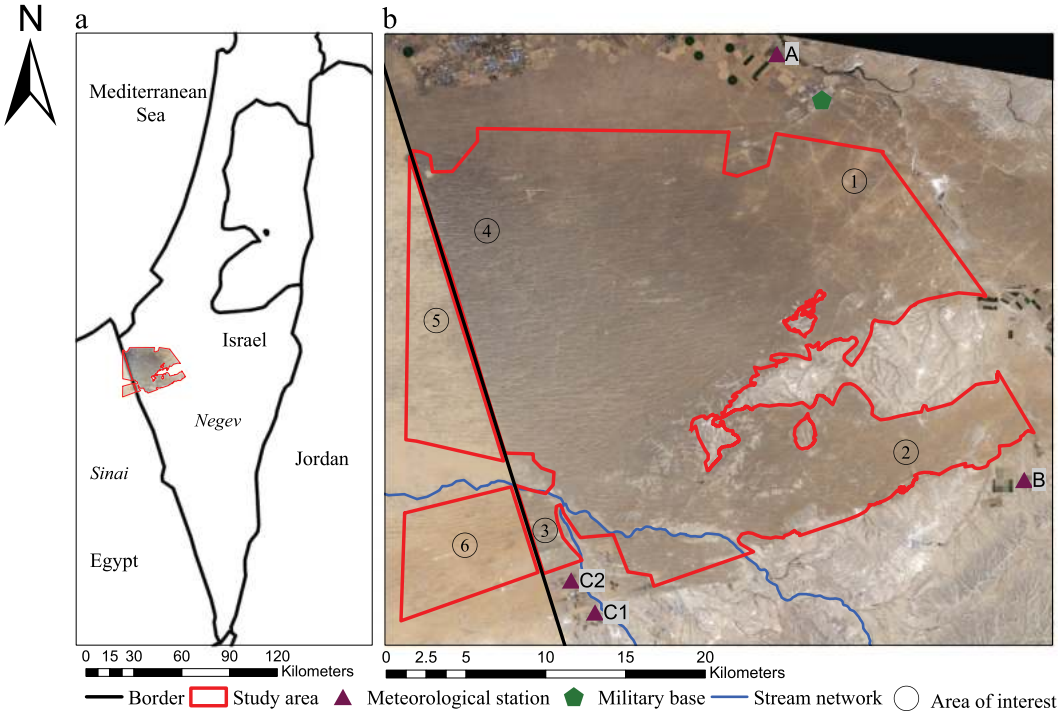

Fig. 1. (a) Location of the sandfield study area, the dune fields in the northeastern Negev (Israel) and northwestern Sinai (Egypt); (b) delineation of the study area over a Landsat true-color image with the location of meteorological stations, wadis, and a military base around the study area. Specific areas of interest (AOI) within the domain include: military training area (1), grazing area (2), nature reserve and military activity area (3,4), areas of civilian, military, and animal activity (5, 6). (For interpretation of the references to color in this figure legend, the reader is referred to the web version of this article.)

1948, the Negev dunes have changed their characteristics and stabilized, while the Sinai dunes have remained active (Karnieli and Tsoar, 1995). Dall'Olmo and Karnieli (2002) and Qin et al. (2006) found that the area west of the border is relatively static, with minimal, if any, temporal changes. There is a clear difference in the reflectance between the two sides of the border, in that the Egyptian side appears much brighter than the Israeli side (Fig. 1b).

Additional effects on the dune stabilization include long-term wet and dry climatic cycles that contribute to the attached cyanobacteria and fine particles, generating widespread biocrust cover over most of the Negev's dunes, particularly along the interdunes and dunes' hillsides. Despite their thin appearance on the surface, a biocrust layer of several mm is enough to protect the sandy dunes from wind erosion (Eldridge and Leys, 2003; Zhang et al., 2006). Different types of microphytes exist along the precipitation gradient of the study area. Mosses, soil lichens, and cyanobacteria are dominant in regions with 200–300 mm (north), 100–200 mm (center), and less than 100 mm (south), respectively (Karnieli et al., 1996; Zaady et al., 2014).

2.2. Data collection

2.2.1. Remote sensing imagery

A series of Landsat 5 TM (1987–2011) and Landsat 8 OLI (2013–2018) summertime images (Fig. 2) were acquired from the USGS (https://earthexplorer.usgs.gov) with a spatial resolution of 30 m, for 31 years between 1987 and 2018, excluding 2012 due to the high presence of cloud cover. The dry season (June to August) was chosen to avoid the reflectance of wet biocrusts, which is very similar to that of vascular vegetation and may cause misinterpretation (Karnieli, 1997). Radiometric and atmospheric corrections were performed using Atcor3 (Richter and Schlapfer, 2019), and the images were processed using the ERDAS Imagine software (https://www.hexagongeospatial.com/products/power-portfolio/erdas-imagine).

2.2.2. Meteorological data

Precipitation data were collected from the Israel Meteorological Service archive and the regional research and development station during the rainy season (October to May) (Fig. 2). Since there are no meteorological stations within the study area, data were compiled from three nearby stations (Fig. 1b).

2.3. Crust Index (CI)

To understand the temporal trends of the biocrusts within the study area, the CI was calculated for the entire set of images (Fig. 2). The CI is the most effective spectral index to identify and map the presence of biocrusts that contain cyanobacteria. It was established on the fact that cyanobacteria contain phycobilin, a pigment that has higher reflectance in the blue spectral band, in comparison to a sandy substrate (Karnieli and Sarafis, 1996). Hence, the spectral index is based on the normalized difference between the reflectance of the red and blue spectral regions (Karnieli, 1997):

$$CI = 1 - \frac{\rho Red - \rho Blue}{\rho Red + \rho Blue} \quad (1)$$

where ρRed and $\rho Blue$ are the reflectance values in the red and blue spectral bands, respectively. The CI values range between 0 and 2 and, more frequently, between 0 and 1. Higher CI values are associated with higher levels of biocrust density. The CI is suitable for characterizing the biocrusts in the study domain since they are mainly composed of cyanobacteria (Karnieli et al., 1996; Zaady et al., 2014).

2.4. Long-term trend analysis

To achieve the first specific objective and quantify long-terms trends to establish which areas went through a significant positive or significant negative temporal change in CI values over 31 years, a Mann-Kendall (MK) trend test was applied to each pixel in the study area (Fig. 2).

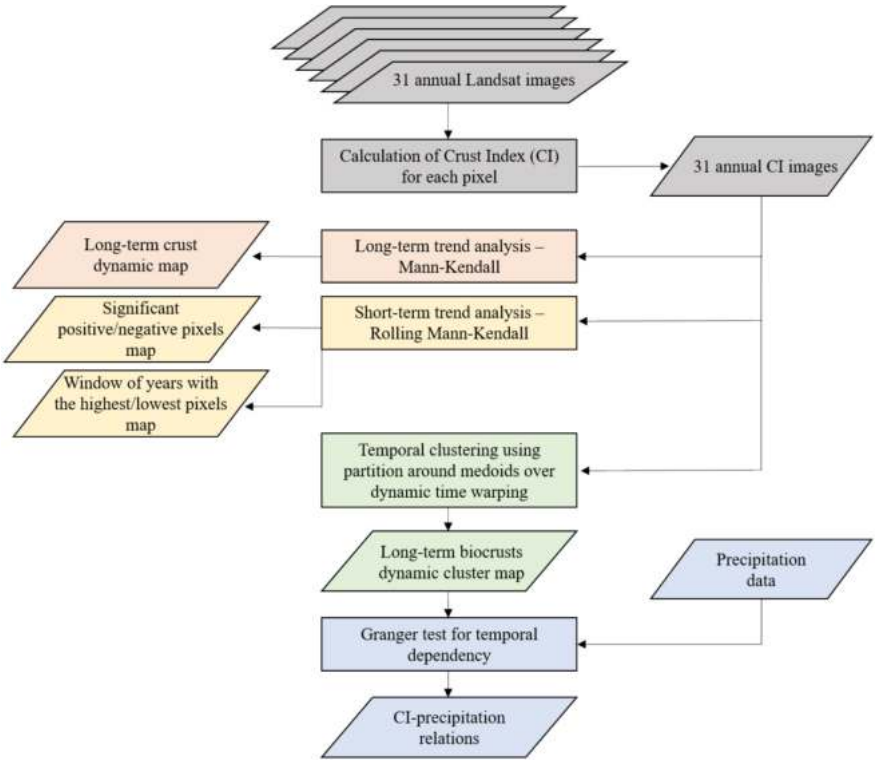

Fig. 2. Flowchart of the study methods. The colors highlight the different stages of the project as subsectioned in the Methodology and Results. (For interpretation of the references to color in this figure legend, the reader is referred to the web version of this article.)

The MK is a common non-parametric trend test that ranks the magnitude and direction of the trend of a variable over time (Mann, 1945; Kendall, 1955). This statistical test considers the rank of the observed values and their position in the time series (Hamed and Ramachandra Rao, 1998). In the current case, the MK test was performed for each vector of one pixel based on its 31 values (31 years) of the CI, such that each pixel resulted in a *Z*-score following a normal distribution; thus, the significance and direction of change could be obtained. The processing of the CI data cube was performed using the '*stars*' package in R (Pebesma, 2020). The MK was calculated using the R package '*trend*' (Pohlert, 2020), and the images were processed using the '*raster*' package in R (Hijmans, 2020). To plot the *Z*-scores for each pixel in space, the R package '*RStoolbox*' was used (Leutner et al., 2019). Visualization was enabled using the R packages '*ggspatial*' (Dunnington, 2020) and '*ggplot2*' (Wickham, 2016). In order to visualize the level of significance and the direction of change for each pixel, reclassification of the Z-scores was implemented, and the levels of significance were arranged into seven classes. The levels include significant negative changes at $\alpha = 0.01$, $\alpha = 0.05$, and $\alpha = 0.1$, significant positive changes at $\alpha = 0.01$, $\alpha = 0.05$, and $\alpha = 0.1$, and no significant change. To evaluate the distribution of significance levels, a histogram was generated, taking the $\log_{10}$ of the frequency of each significance level.

2.5. Short-term trend analysis

To fulfill the second objective, analyzing the short-term trend for a vector of each pixel in the study site, a calculation of MK was performed over a moving window of five years, resulting in a total of 27 windows, thus providing a rolling statistic (Z-score) over time. This approach was used to achieve temporal trends for short intervals. For each window, the MK test was calculated, resulting in a Z-score, signifying the magnitude of change, its significance level, and the direction (positive or negative) during each sub-period of five years (Fig. 2). This analysis was applied using the R package '*trend*' (Pohlert, 2020). The rolling MK test enabled periodic evaluation of the temporal trend, such as increased crust development during certain time intervals in specific locations, compared to different extents of decrease. With the Z-score result for each pixel over the 27 temporal windows, four different maps were produced to illustrate the spatial and temporal trends. The first and second maps present the maximum and minimum values of significant Z-scores for each pixel over time, respectively. In addition, the third and fourth maps provide, at the pixel level, the window for which the maximum and minimum Z-score values were received, respectively. The maps were generated using the R package '*stars*' (Pebesma, 2020) for managing the array of raster layers and '*ggR*' (Leutner et al., 2019) for visualization.

2.6. Temporal clustering

To achieve the third objective and gain a deeper understanding of the spatiotemporal dynamics over 31 years across different regions (within the study area) and to analyze the factors that led to a change, temporal clustering of the CI time series was performed (Fig. 2). A temporal clustering analysis can be performed using various mathematical methods in an attempt to detect similar items in a dataset and group them together (Romesburg, 2004). The dataset in the study area included 31 images with more than 1.5 million pixels in each image, making the temporal clustering process computationally intensive. In order to perform a cluster analysis on the CI values over time using efficient computational resources, 10,083 points in space were randomly sampled from the entire set of pixels within the study area, corresponding to a confidence level of 95% and a confidence interval of one. The multi-annual CI values were then extracted for each sampled pixel, resulting in a temporal vector of CI values.

To partition certain pixels into similar groups, there was a need to quantify similarities and dissimilarities among sampled pixels. The distance matrix provides a dissimilarity (distance) measure for each pair of sampled pixels and the clustering relies on these distances, while

sampled pixels with smaller distances are assigned to the same cluster. A distance matrix was computed for the CI values for each pair of sampled pixels using dynamic time warping (DTW) (Berndt and Clifford, 1994). DTW is a technique designed to find an optimal conformation between two given time series and is used for time deformation of different patterns. The technique uses dynamic programming to align two time series vectors of a specific segment in time so that the distance measure is minimized. The pattern detection of the first time series needs to contain instances from the second time series (Berndt and Clifford, 1994). The DTW technique was implemented using the '*dtwclust*' R package (Sarda-Espinosa, 2019).

By clustering pixels with high levels of similarities through time, different spatial patterns of temporal characteristics in the study area can be revealed. The partition around the medoids (PAM) algorithm was used for clustering. This technique assigns a representative object, or medoid, for each cluster. This means that each cluster may be expressed by a pixel that is most similar to all other members of the cluster over time (Kaufman and Rousseeuw, 2009), namely a cluster center. PAM was applied to the sample size (10,083 pixels), using the '*cluster*' package (Maechler et al., 2019).

The optimal number of clusters, *C*, was selected based on the highest average silhouette width (ASW) value after examining a range of $3 \le C \le 8$ clusters. The ASW indicates how "natural" the clustering is, meaning that the sampled pixels within the cluster are similar to each other, whereas there are fewer similarities between the clusters (Kaufman and Rousseeuw, 2009). The dissimilarity index was used to assess the goodness of the clustering model. The R package '*clusterCrit*' (Desgraupes, 2018) was used to compute the ASW.

The following step assigned the entire set of pixels in the study area to their respective clusters, by applying the RF classifier. RF is a machine learning algorithm that is implemented for regression and classification problems; it classifies each node using the best split among a group of randomly chosen predictors, which are the training samples (Liaw and Wiener, 2002; Pal, 2005). The RF classifier involves a set of tree-structured classifiers, where every decision tree continues to grow through random training points until it reaches the number of trees that were predefined (Breiman, 2001; Chen et al., 2019; Liaw and Wiener, 2002). The RF classification was conducted using the R package '*randomForest*' (Liaw and Wiener, 2002).

In order to evaluate the performance of the RF classification, the sampled pixels used for the PAM algorithm (10,083) were used as training data. An additional testing set (4217) of sampling points was randomly selected from the remaining study area. The performance of the RF model was evaluated using the confusion matrix-based measures' overall accuracy and the Kappa coefficient. The training procedure was evaluated using an estimated error rate. To analyze the changes in space over time, a cluster map was created, using the '*RStoolbox*' package in R (Leutner et al., 2019), presenting groups of pixels in which the CI values changed similarly over 31 years. The trend of each cluster over time was illustrated using the values of the cluster centers. The plots were produced using the R package '*ggplot2*' (Wickham, 2016). In order to present differences between the clusters, the mean, standard deviation (SD), and coefficient of variation (CV) were calculated for each cluster. All cluster centers were evaluated in order to avoid temporal autocorrelation, to ensure that parametric tests may be applied. Correlations were calculated for every paired cluster center to assess the association between them over time. A *t*-test was applied for all paired combinations of cluster centers in order to verify significant differences between the cluster center means. The Kolmogorov-Smirnov (Lilliefors, 1967) test between all paired cluster centers was used to check the similarity between distributions.

2.7. Biocrust response to rainfall

Relations between the different CI cluster trends and precipitation levels were investigated using the Granger Causality test (Diks and Panchenko, 2006; Granger, 1969) (Fig. 2). The Granger Causality test finds the relationship between two time series when one precedes the other. The null hypothesis is that one time series is not related to the other time series and the relation is random (Granger, 1969). The time series of yearly rainfall was monitored by three meteorological stations, as specified in Subsection 2.2.2 (Fig. 1). The yearly precipitation amounts were acquired for the winter period in Israel. The time series of both the multi-annual rainfall and the CI cluster centers were smoothed using the non-parametric local regression (LOESS) algorithm, with 0.4 as the degree of smoothing (Kneip et al., 2000; Zhang and Liu, 2006). Then, the smoothed curves of rainfall and CI values were normalized in order to set the curves to the same scale using the empirical cumulative distribution function (ECDF). The smoothing and normalization were conducted using R (R Core Team, 2020). The Granger Causality test was applied to every combination of the three cluster centers with the time series acquired from the three different stations.

3. Results

3.1. Time series visualization of the Crust Index

The CI time series is presented as a simple mapping of all 31 yearly images of the study area, including only the sandfields (Fig. 3). The CI values in the study area ranged between 0.5 in areas with low biocrust levels and up to 0.8 in areas with high biocrust density. The contrast between the Israeli and Egyptian sides of the border over the years is constant through time. The area on the Israeli side closest to the border, area of interest (AOI) 4, consisted of the highest CI values in most years. Distinct gradients were found, decreasing from north to south and west to east. Finally, an overall decrease in the CI values over time may be visualized, as there are more pixels with low CI values (red) and fewer pixels with high CI values (blue), over time.

3.2. Long-term trend analysis

The direction and magnitude of change in the CI that each pixel experienced over 31 years (1987–2018) within the study area was analyzed using the MK trend test. To illustrate the direction, magnitude, and significance of the trend, a *Z*-score map (Fig. 4a) and a complementary histogram (Fig. 4b) were generated. The thematic map presents the level of significance of the temporal trend for each pixel in space over time. The map that was generated, based on the MK trend test calculated for each pixel, determined that the areas with the highest percentage of pixels that experienced no significant change were located on the Israeli side. These were grouped in two visible sites in the northwestern (AOI 4) and southwestern (AOI 3) regions of the Israeli side of the border. Some patches of non-significant change were also dispersed in the eastern region of the study area (AOIs 1 and 2). The areas that experienced a positive change in CI values were spread around the study area in small patches, on both sides of the border. Positively changed CI pixels were also visible in the area near AOI 3. There was a notable general decrease in CI levels in the study area, as seen in Fig. 4a, while a large portion of the region experienced significant negative long-term change. The histogram presents the $\log_{10}$ of the frequency of the pixels in the study area for each level of significance; while 88.7% of the pixels experienced significant negative changes ($\alpha \le 0.1$), 10.8% showed no change, and 0.5% experienced significant positive changes.

3.3. Short-term trend analysis

Since the long-term analysis presented an overall decrease in the study area, a complementary analysis was conducted to highlight short-term trends. The MK calculation of the CI vector for each pixel was performed using a moving window of five years, resulting in a total of 27 windows, thus providing a rolling statistic over time. A *Z*-

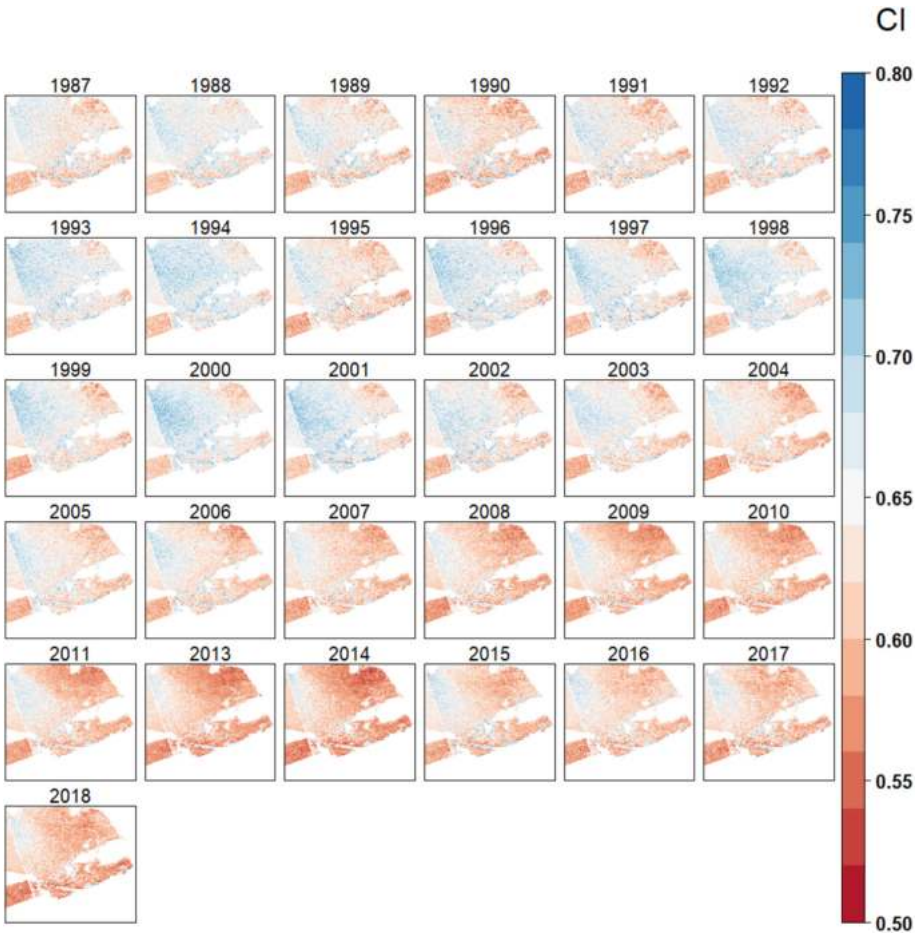

Fig. 3. Time series of masked Crust Index (CI) maps. High CI values are presented in blue, and low CI values are presented in red. (For interpretation of the references to color in this figure legend, the reader is referred to the web version of this article.)

score was calculated for each window, signifying the magnitude of the change, its significance level, and direction (positive or negative). Fig. 5 shows the Z-score map for each five-year window. Until the window of 1999–2003, most pixels were characterized by a positive change. Then, between the windows of 2000–2004 and 2009–2014, most of the region experienced a negative change in the CI. The window of 2010–2015 shows mostly a no-change/positive trend again until the end of the study period.

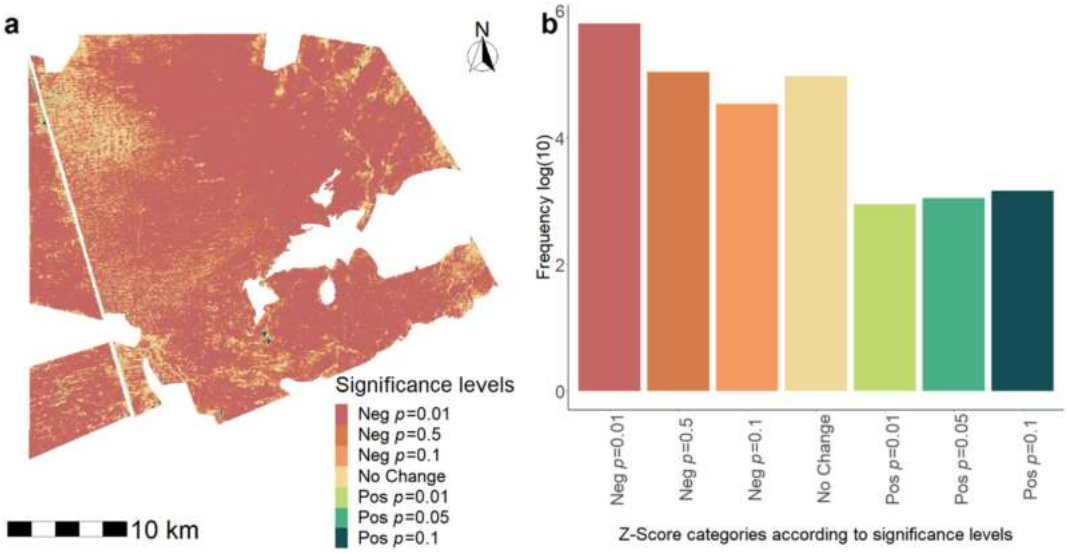

Fig. 4. (a) The level and direction of significance for each pixel over time, following the Mann-Kendall trend test; (b) histogram of the frequency (log10) of the pixels for each level of significance shown in map a.

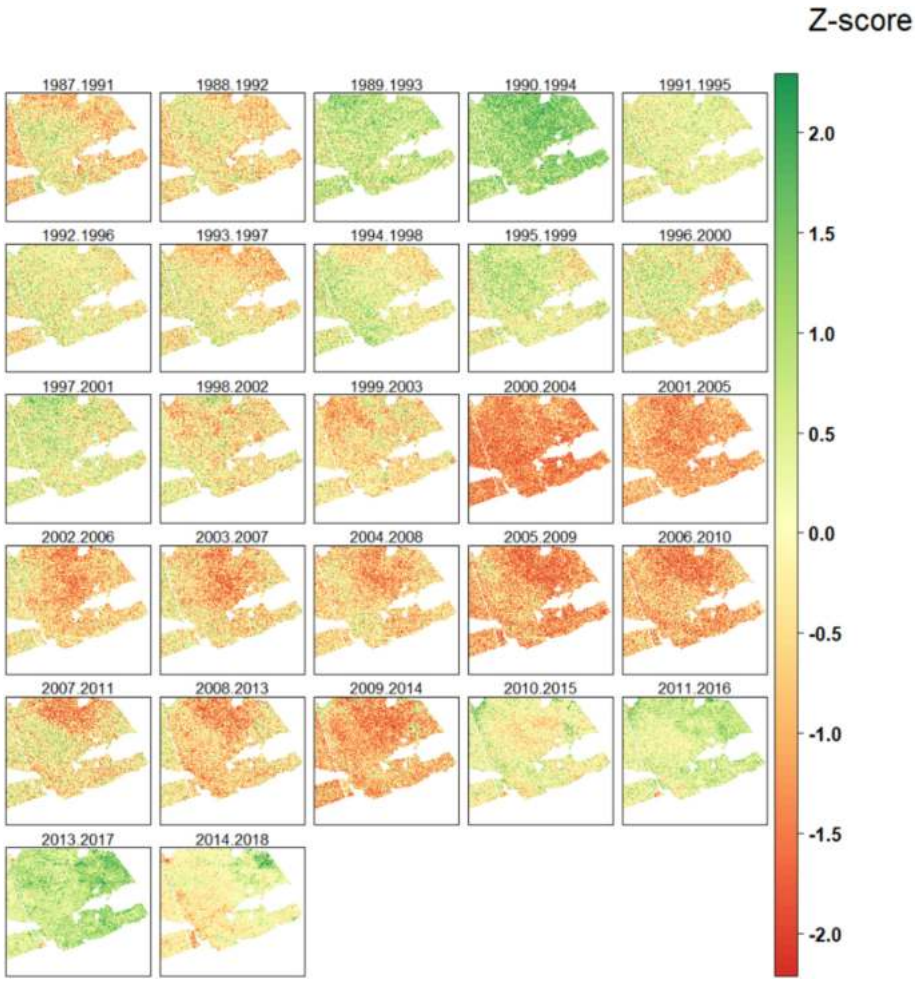

Fig. 5. Z-score maps based on the Mann-Kendall trend test of Crust Index values. Each map represents a window of five years. Reddish color represents negative changes, while greenish represents positive changes. (For interpretation of the references to color in this figure legend, the reader is referred to the web version of this article.)

Figs. 6 and 7 show extreme (minimum and maximum) levels of change on the two sides of the border and a general shift in trend from east to west. Significant positive and negative changes in the MK test can be visualized with maps that represent the significant lowest and highest Z-score levels for each pixel over 27 windows (Fig. 6). The highest and lowest Z-score values from the five-year windows were assigned to each pixel, while only the significant values are presented in the maps (both positive and negative). Fig. 6a depicts the highest Z-

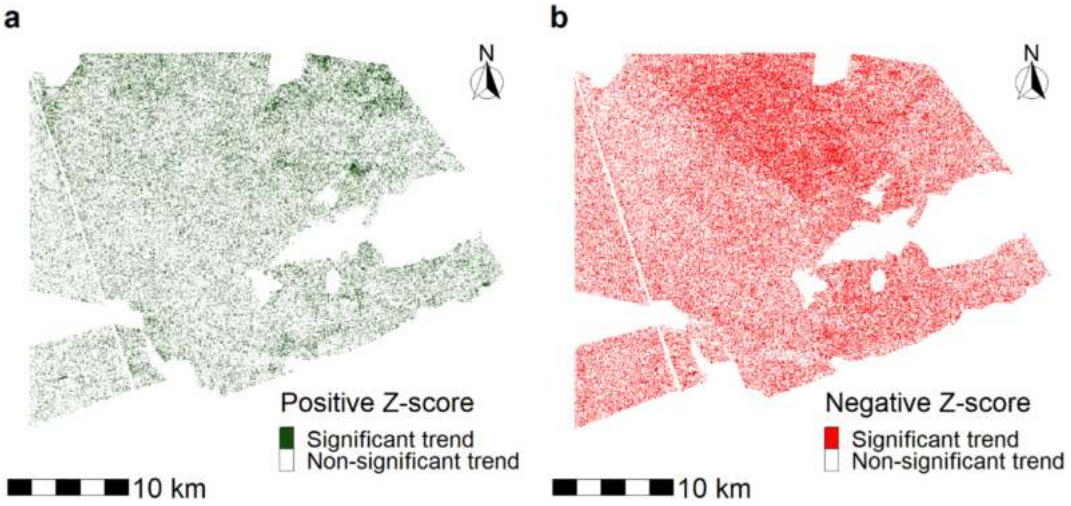

Fig. 6. Z-score maps based on a five-year window rolling Mann-Kendall trend test of the Crust Index: (a) significant positive Z-score received out of all short-term trend windows during the time period (1987–2018) for each pixel; (b) significant negative Z-score received for each pixel. White pixels represent insignificant (positive and negative in panels a and b, respectively) values.

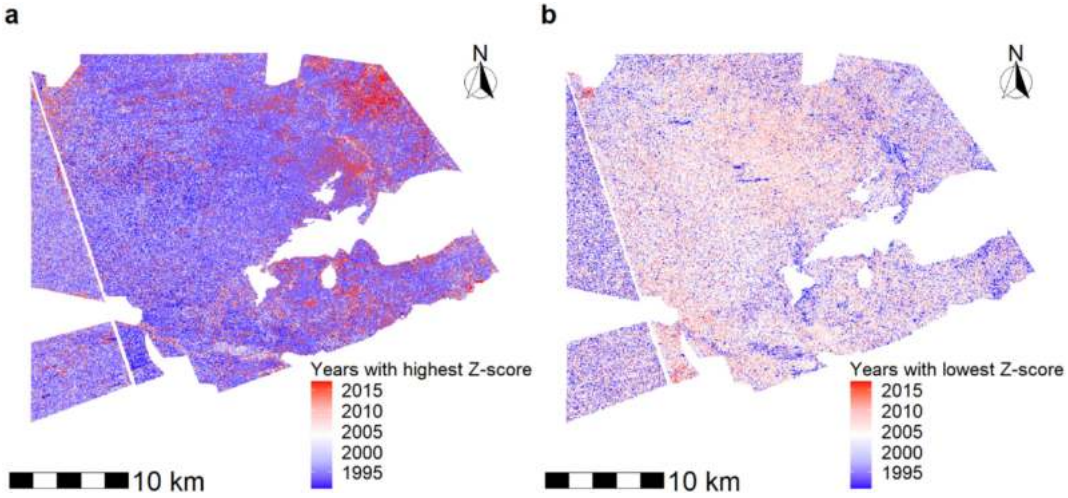

Fig. 7. Z-score maps illustrating the five-year windows of extreme changes in the Crust Index, quantified using the Mann-Kendall trend test for (a) maximum Z-score values; and (b) minimum Z-score values. Blue represents earlier years, while red represents later years in the study's timeframe. The year labels stand for the first year of the five-year window. (For interpretation of the references to color in this figure legend, the reader is referred to the web version of this article.)

score per pixel and signifies the maximum change during all short-term trend windows. Significant changes are shown in the northeast (AOI 1) and northwest (AOI 4) regions of the study area, resulting in a north to south gradient. Positive significant Z-score pixels also characterize the southwestern area next to the border in Israel (AOI 2). In Fig. 6b, which presents the lowest significant lowest Z-score value per pixel, there is a stronger level of homogeneity throughout the study area. However, in the central region of the study area, there is a high density of pixels that experienced a strong significant negative change.

To understand the window of years during which the strongest negative and positive trends occurred, two maps were generated (Fig. 7). Fig. 7a represents, for each pixel, the window of years for which the highest Z-score values were computed, while Fig. 7b depicts the years of the lowest Z-score values. High levels of positive change characterized the early years in our study period, while high levels of negative change were determined in the later years. In Fig. 7a, many positive Z-scored pixels were defined in the far eastern part (AOI 1) during the late years of the study's timeframe. In general, there were mainly positive changes during the 1980s and the 1990s. On the Israeli side, more areas experienced various degrees of positive change from 2005 to 2018, especially closer to the border. Some late positive changes were observed on the Egyptian side, close to the border (east to AOI 5). Fig. 7b represents the window of years consisting of the lowest Z-score value for each pixel and shows some contrast between the western and eastern sides of the study area. The blue color represents negative change during the late 1980s, while the Israeli side is characterized by negative change later in time, between 2000 and 2010.

3.4. Temporal clustering

To analyze the changes in space over time, a temporal cluster analysis was performed considering a temporal vector of CI values for each pixel in the study area. Fig. 8 represents groups of pixels within which CI values changed similarly over 31 years. The clustering of the area can highlight both spatial (Fig. 8a) and temporal (Fig. 8b) information that can lead to a better understanding of the environmental and anthropogenic factors causing the diverse long-term trends of change. The optimal number of clusters was three, selected according to the highest ASW value (ASW = 0.33). The ASW values for the three clusters were 0.30, 0.37, and 0.38 for Clusters 1, 2, and 3, respectively. The

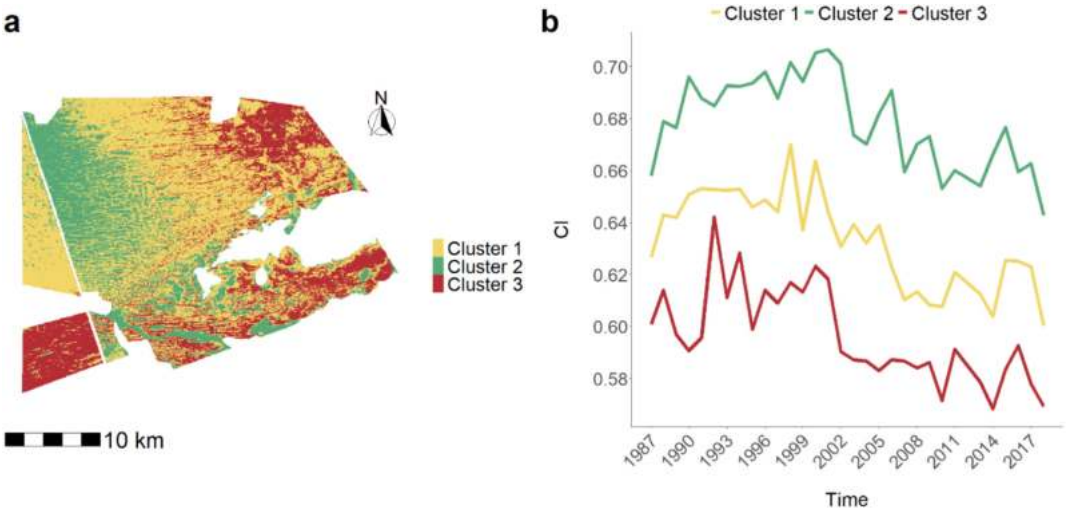

Fig. 8. Cluster analysis of the Crust Index time series: (a) cluster map divided into three different clusters, each representing different trends of the Crust Index through time; and (b) time series of the corresponding cluster centers (medoids of each cluster).

Table 1
Confusion matrix for the training set after applying the Random Forest model.

Reference/prediction	Training samples Cluster 1	Training samples Cluster 2	Training samples Cluster 3	Class error
Training samples Cluster 1	4918	72	85	0.030
Training samples Cluster 2	97	2321	0	0.040
Training samples Cluster 3	153	0	2437	0.059

training set of the RF model had an estimated error rate of 4.04%, the overall accuracy of the RF classifier using the test set was 0.96, and the Kappa coefficient was 0.93. The confusion matrix of the RF classification is presented in Tables 1 and 2. It appears that pixels from Cluster 2 were not assigned to Cluster 3, and pixels from Cluster 3 were not assigned to Cluster 2, both in the training samples and the test samples. In contrast, Cluster 1 did include pixels from Clusters 2 and 3. This means that Cluster 3 was the best classified, and Cluster 1 was the worst classified.

Fig. 8 presents the dynamics of the three clusters in space and time. In terms of the spatial trend (Fig. 8a), there was an evidential difference between the two sides of the border and the western and eastern parts of the Israeli side. Also, there was a substantial difference between the northern area of interest (AOI 5, Fig. 1) and the southern (AOI 6) parts of the study site on the Egyptian side. The CI values in the northern part were assigned to Cluster 1, while the south was characterized by CI values assigned to Cluster 3. On the Israeli side of the border, the spatial patterns of the CI's temporal dynamics are mixed. The northernmost (AOI 4) and southernmost (AOI 3) regions that are closer to the border are characterized by the highest values over the years. In the northeast, the area near the military training base (Fig. 1) is attributed to Cluster 3. To a lesser extent, there were areas on the Egyptian side of the border that also consisted of a higher CI value (Cluster 2). A time series of each cluster center is presented in Fig. 8b. The three cluster centers have similar decreasing patterns through time, but their fluctuation patterns differ, as well as their CI levels. Cluster 1 consists of moderate CI values, ranging from 0.60–0.67. The CI values of the areas assigned to this cluster showed an overall increase until 2000 and then slowly decreased until an upward trend began in 2015. Cluster 2 was characterized by the highest CI values (0.64–0.71). The CI values of the regions assigned to Cluster 2 remained the highest over the years and started to decrease in 2002. Cluster 3 had the lowest CI values, ranging from 0.58–0.64. The regions assigned to Cluster 3 experienced a moderate increase in CI levels until 2000 and then showed a drastic decrease, with constant low values since then.

For each cluster, the mean, SD, and CV were calculated and are presented in Table 3. The highest mean CI value was for Cluster 2, followed by Clusters 1 and 3. The SD and CV of all the clusters were similar. Several statistical tests were performed to distinguish between the temporal dynamics of the different clusters. The interactions between the three different cluster centers are summarized in Fig. 9, including a correlation coefficient (r) between each pair of cluster centers, a t-test, and the Kolmogorov-Smirnov test (D). High correlation was found between the cluster centers of Clusters 1 and 2 ($r = 0.80$). The correlation between the centers of Clusters 1 and 3 ($r = 0.79$) was slightly smaller than the correlation between the centers of Clusters 1 and 2, and the correlation between Clusters 2 and 3 was the lowest ($r = 0.67$). All cluster centers had significantly different CI means, as well as distinct distributions.

3.5. Biocrust response to rainfall

The relations between the three smoothed and normalized cluster centers and the smoothed and normalized multi-annual precipitation were quantified using the Granger Causality test. The highest responses of the cluster centers' CI values to the multi-annual rainfall amounts were found for a lag of one year. A significant response was found between the yearly rainfall in meteorological station B and all the clusters' centers (Table 4). Cluster centers 1 and 3 had significant relations with the rainfall measured in meteorological station C, while cluster center 3 had a significant response to the rainfall in meteorological station A through time.

4. Discussion

In this study, we evaluated the CI trend through time between 1987 and 2018, across the area surrounding the border between Israel and Egypt. Local changes and spatial patterns of temporal dynamics were detected using various statistical models. Different regions in the study area experienced different CI trends over time due to anthropogenic and climatic factors. While investigating the long-term trend, a noticeable decrease in the CI levels over most of the area was found, with 88.7% of pixels experiencing a significant negative change and only 0.5% experiencing a significant positive change (Fig. 4). The ability to divide the period of 31 years into 27 rolling windows of five years enabled the areas that experienced significant change during a narrow time window to be highlighted. The division into smaller sections of time may assist in defining the different changes and their contributing factors. Combining statistical methods of analyzing the CI, over the long term, short term, and clustering over time, may highlight trends during various time frames, as well as helping to compare the temporal dynamics throughout the area. For instance, the military training area (AOI 1) is assigned to Cluster 3 and has low CI values across time (Fig. 8), but it has shown a strong positive trend since 2011 (Fig. 7a). The increase in CI values in the later years on the Egyptian side is also visible in the

Table 2
Confusion matrix for the test set after applying the Random Forest model.

Reference/prediction	Test samples Cluster 1	Test samples Cluster 2	Test samples Cluster 3	Class error
Test samples Cluster 1	2067	56	58	5.22
Test samples Cluster 2	29	941	0	2.98
Test samples Cluster 3	38	0	1028	3.56

Table 3
Descriptive statistics for each cluster, including the mean, standard deviation (SD), and coefficient of variation (CV).

Descriptive statistic	Cluster 1	Cluster 2	Cluster 3
Mean	0.63	0.67	0.59
SD	0.018	0.017	0.018
Coefficient of variation	0.028	0.025	0.030

short-term analysis (Figs. 6, 7) but does not appear in the long-term analysis. The easternmost side of the study site (AOI 1) and the southwestern part of the Egyptian side (AOI 6) were characterized by significantly lower CI values than other regions in the study area (Figs. 8, 9). In the eastern part of the study area, the continuous decreasing trend in the CI (Fig. 5) was due to the effects of military training activities. These military activities prevent biocrust establishment and lead to soil degradation (Zaady et al., 2016). Military training involves vehicle maneuvers that increase the percentage of bare soil and delay cyanobacterial recovery. The effects of military activities on the ecological system, in general, and on biocrusts, specifically, through time have been documented in a few studies (Belnap and Warren, 2002; Prosser et al., 2000; Zaady et al., 2016), showing that maneuvering of land vehicles has a severe impact on the biocrusts. In recent years, there were some positive changes in CI levels (Figs. 5, 7a) due to fewer off-road vehicles (Johnson et al., 2009; Solescu, 2020), causing less disruption to the surrounding area. The clear difference between the two sides of the border during the entire time period examined was most likely due to trampling by humans and farm animals on existing crust and the prevention of new crust accumulation across the southern Egyptian side (Karnieli and Tsoar, 1995; Kidron, 2016). In contrast, the protection policy on the Israeli side presented an opportunity for biocrusts to be established and continue developing (Karnieli and Tsoar, 1995). In recent years, since 2013, when a barrier between Israel and Egypt was constructed (Vallet, 2016), biocrust development around the border has increased on both the Israeli side and the Egyptian side (Figs. 4a, 7a). The area on the Israeli side closest to the border (AOI 4) consisted of significantly higher CI values than other regions of the study area during most of the years (Figs. 8, 9), due to limited anthropogenic activities and protection of this region by the Israel Nature and Park Authority. The conservation efforts resulted in constant CI levels (mostly no significant change) and some positive change over the years in the area east of the border (Fig. 4a). In the southeastern part of the study area (AOI 2), there was a constant negative change with patches characterized by positive change over the years (Figs. 4a, 8a). Positive changes were possibly due to the short distances from the stream network that enabled access to water and higher soil moisture levels that enabled biocrust development (Wilcox, 2010; Yair, 1990; Zaady et al., 2014), while simultaneously, intense overgrazing over time led to negative changes. The overgrazing may be explained by a new Bedouin settlement established in 1993 and legalized in 2012 (Shmueli and Khamaisi, 2015). The Bedouin village relies on herds of sheep and goats as part of their livelihood, leading to soil trampling and biocrust destruction (Karnieli and Tsoar, 1995) in the southeastern part of the study area.

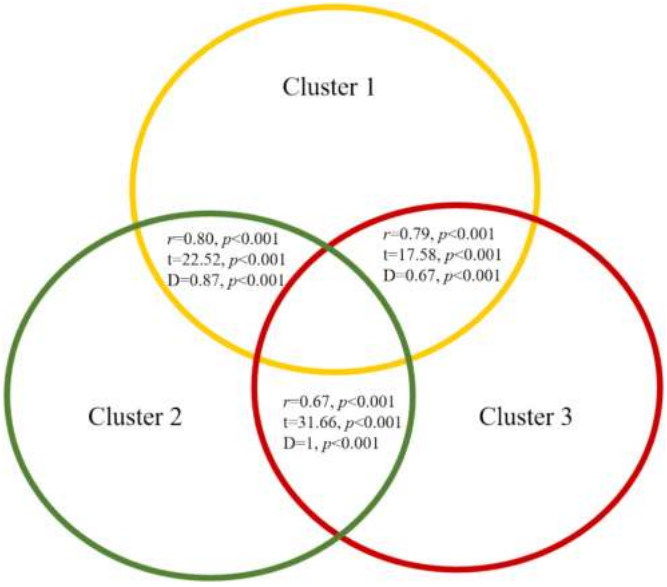

Fig. 9. Summary of the statistical differences between all pairs of cluster centers of the three clusters, including correlation (r), *t*-test (t) and the Kolmogorov-Smirnov test (D), followed by corresponding *p*-values.

Table 4
Granger Causality (lag = 1) results for smoothed and normalized CI cluster centers and smoothed and normalized multi-annual rainfall measured by three different meteorological stations across the study area. Significant relations are presented in bold.

	Cluster center 1	Cluster center 2	Cluster center 3
A	$F = 2.99$	$F = 2.94$	$F = 4.75$
	$p = 0.09$	$p = 0.09$	$\mathbf{p < 0.05}$
B	$F = 16.43$	$F = 13.60$	$F = 9.60$
	$\mathbf{p < 0.001}$	$\mathbf{p < 0.01}$	$\mathbf{p < 0.01}$
C	$F = 6.96$	$F = 2.04$	$F = 5.72$
	$\mathbf{p < 0.05}$	$p = 0.15$	$\mathbf{p < 0.05}$

The clustering model provided reliable results (ASW = 0.33 for the PAM model) with a strong performance of the RF classifier (a total error rate of 4.04% for the training samples with an overall accuracy of 0.96 and Kappa = 0.93 for the test samples). Clustering of the area can highlight both spatial and temporal patterns of biocrust distribution that may lead to a better understanding of the environmental and anthropogenic factors causing the diverse short- and long-term trends of change. Each cluster (Fig. 8) indicates a different temporal pattern that characterizes the assigned pixels over 31 years. The plot in Fig. 8b depicts the temporal dynamics of the cluster centers. Clusters 2 and 3 achieved the best result of similarity with ASW of 0.37 and 0.38, respectively, and Cluster 1 had the lowest ASW of 0.30. These results indicate that Cluster 3 was best clustered, followed by Clusters 2 and 1, according with the result that Cluster 1 is intermediate, in that it is spatially located between Clusters 2 and 3. The spatial gradient from high CI values (west) to low values (east) (Fig. 3) leads to a stronger association between regions with similar temporal CI trends at the margins of this gradient (Clusters 2 and 3), and lower clustering results in the transition zone (Cluster 1). Although the findings show significantly different patterns in the CI values of the cluster centers (Fig. 9), there was a strong association in temporal trends between all clusters ($0.67 \le r \le 0.8$). These similarities include a moderate increase in CI levels from 1998 to 2000 and then a decrease in all the clusters until 2010 (there are fluctuations between the years, but the trend is uniform). Between 2010 and 2018, there was a similar trend of increasing CI levels until 2011, a decrease until 2014, an increase again until 2017, followed by a decrease. The similarities in the general trends of the cluster centers throughout the study area are most likely due to meteorological factors affecting biocrust development and growth over time. Relations between CI levels and rainfall amounts were studied using datasets from three different meteorological stations located close to the study area. Significant relations were found between rainfall and CI levels in six out of nine cases (Table 4). Our findings accord with previous studies that related annual rainfall amounts to biocrust establishment and stabilization (Weber et al., 2016). Higher levels of water availability promote the development of new cyanobacterial colonization, which is a component of biocrust (Zaady et al., 2014). Yair et al. (2011) indicated

that the average rainfall amount controls the small changes in the biocrusts and the surface properties. While a decrease in precipitation can negatively affect the thin layer of biocrust and cause degradation, an increase in water availability can increase the water concentration in the topsoil and maintain water in the deep soil, thus promoting biocrust development. Yair et al. (2011) and Zaady et al. (2014) presented a relationship between the bio-physiological characterization of the biocrust properties and climate change scenarios that may affect the aridity levels of the area along multiple gradients (such as the rainfall gradient, sedimentological gradient, biological gradient, etc.). These studies are in line with our findings, in which significant relations between rainfall and the CI levels appeared across most of the study area. However, it should again be noted that the meteorological stations were not located within the study area. Meteorological stations in arid regions are usually sparsely distributed, often making meteorological data in arid lands unavailable, with a low spatial representation that is often incomplete (Ahmed et al., 2019; Karnieli et al., 2014). The temporal analysis in the same study area in previous studies was limited to up to four consecutive years (1994–1998) and involved ground and NOAA-AVHRR-derived vegetation indices and land surface temperature (Dall'Olmo and Karnieli, 2002; Karnieli et al., 2002). In the current project, however, the time period investigated is long and includes 31 years (1987–2018).

The persistence of the biocrusts in the sandfield across the Israel-Egypt border has drawn the attention of many scientists since the mid-1970s (e.g., Otterman, 1974). To the best of our knowledge, all studies, until the current, were restricted to several kilometers, mostly on the eastern side of the border (e.g., Karnieli and Tsoar, 1995; Qin et al., 2001; Tsoar and Karnieli, 1996). The CI has been widely researched, both globally and across the Israel-Egypt border, with a strong focus on the spatial variability of biocrusts. Hill et al. (2008) stated that a high degree of spatial variability in the current study site exists, based on biocrust monitoring using remotely sensed imagery. Paz-Kagan et al. (2014) investigated the spatial distribution of the CI through time using remote sensing retrievals in order to detect the spatial patterns of structural temporal changes in desertified shrublands. There has been a strong interest in biocrusts' spatial variability and distribution patterns. This present study relies on these previous findings and extends the knowledge regarding biocrust spatial variability and its association with anthropogenic factors, i.e., military activities, overgrazing, conservation policies, etc.

Land cover and land use changes are caused by various phenomena in space. In arid environments, biotic components are highly sensitive to anthropogenic effects and land use changes (Ohana-Levi et al., 2019; Wilcox et al., 2011). Anthropogenic mechanisms that promote the loss and degradation of the soil surface habitat include military training that involves off-road vehicles and tanks, artillery training, construction of sideroads, camping activities, and other touristic activities (Zaady et al., 2016). In a study that was conducted in a military base in North Dakota, Prosser et al. (2000) found that the effect of tracked vehicles can increase the percentage of bare ground by approximately 17%. Belnap and Warren (2002) examined the recovery of cyanobacteria 55 years after they were affected by military training in large areas in the California desert and found that the cyanobacterial component in the biocrust showed a recovery rate of just 46–65% of their biomass in comparison to areas that were not affected by the heavy vehicles. From a meteorological point of view, Siegal et al. (2013) assumed that mobile dunes will replace the biocrust if the average rainfall amount on the southern side of the sandfield is around 50–60 mm and human and animal trampling continues.

Temporal analyses in environmental studies that take place in arid environments using remote sensing retrievals can shed light on biological shifts and their causes (Ohana-Levi et al., 2019). Land use changes in drylands are known to have a strong impact on flora and fauna, and full recovery is nearly impossible (Sivakumar, 2007). It is widely established that some drylands worldwide are undergoing land degradation and desertification due to climate change and anthropogenic impacts (Sivakumar, 2007; Solangi et al., 2019). These causes of change may include overgrazing (Hein, 2006; Hoffmann et al., 2008; Kidron, 2016), nutrient mining (Henao and Baanante, 2006; Lal, 2009; Stones and Treed, 2006), soil erosion (Hill et al., 1995; Ravi et al., 2010; Yang et al., 2003), urbanization (Kosmas et al., 2013; Weng and Lu, 2008), and strong meteorological fluctuations (Puigdefábregas, 2005; Ravi et al., 2010). Drylands have proven to be sensitive to anthropogenic and climatic changes that may introduce ecological imbalances and cause disturbance to the ecosystem (Chapin et al., 2009; Ravi et al., 2010; Smith et al., 2019). Commonly, these natural disruptions are irreversible (Chapin et al., 2009).

5. Conclusion

The goal of this study was to develop a unique framework for analyzing the spatiotemporal dynamics of biocrusts, based on 31 years of satellite imagery. The findings suggest that biocrust dynamics may be altered locally due to anthropogenic factors and regionally due to climatic attributes. The information extracted using complex modeling applied to remote sensing data may lead to a better understanding of the factors that caused these changes during specific periods. A comprehensive overview of biocrusts' spatiotemporal patterns was achieved using an integrative approach that included multiple analyses. In the current study, the modeling frameworks used for meeting the research objectives included analyzing both the long-term and short-term trends of CI dynamics. Additionally, a clustering analysis was performed to define similarities in temporal patterns at a regional scale, and a relationship was found between these patterns and temporal precipitation variations across the study area. The spatial and temporal changes may have been caused by environmental factors, such as precipitation levels or anthropogenic factors, such as overgrazing, military training activities, and conservation practices. The latter were found to induce biocrust rehabilitation. In this current study, we presented a framework to analyze long- and short-term temporal processes and their spatial distribution, as well as an analysis of temporal similarities across space. Combining statistical and machine learning methods for analyzing trends and shifts of long- and short-term series, as well as relating temporal patterns in space, may highlight both specific and general trends. The framework that was proposed in this study may be applied in different studies in the future, using different kinds of indices of spatiotemporal remote sensing retrievals.

CRediT authorship contribution statement

Klil Noy: Writing – original draft, Conceptualization, Methodology, Visualization, Software, Investigation. **Noa Ohana-Levi:** Conceptualization, Methodology, Visualization, Writing – review & editing, Software. **Natalya Panov:** Software, Data curation. **Micha Silver:** Software, Methodology, Writing – review & editing. **Arnon Karnieli:** Conceptualization, Writing – review & editing, Supervision.

Declaration of competing interest

The authors declare that they have no known competing financial interests or personal relationships that could have appeared to influence the work reported in this paper.

Acknowledgments

This project has received funding from the European Union's Horizon 2020 research and innovation program “European Long-Term Ecosystem, Critical Zone and Socio-Ecological systems Research Infrastructure PLUS” (eLTER PLUS) under grant agreement no. 871128. The authors wish to thank Mr. Amiram Cohen and Ms. Shir Triki from the Israel Nature and Parks Authority (NPA) for their valuable insights,

collaboration, and information sharing. The authors would also like to thank Dr. Yael Friedman-Levi for her infographical insights and suggestions. The authors greatly appreciate the support and assistance provided by Dr. Timea Ignat.

References

Aghabozorgi, S., Seyed Shirkhorshidi, A., Ying Wah, T., 2015. Time-series clustering - a decade review. Inf. Syst. https://doi.org/10.1016/j.is.2015.04.007.

Ahmed, K., Shahid, S., Wang, X., Nawaz, N., Najeebullah, K., 2019. Evaluation of gridded precipitation datasets over arid regions of Pakistan. Water (Switzerland) 11 (2). https://doi.org/10.3390/w11020210.

Bayarjargal, Y., Karnieli, A., Bayasgalan, M., Khudulmur, S., Gandush, C., Tucker, C.J., 2006. A comparative study of NOAA-AVHRR derived drought indices using change vector analysis. Remote Sens. Environ. 105, 9–22. https://doi.org/10.1016/j.rse.2006.06.003.

Belnap, J., Warren, S.D., 2002. Patton's tracks in the Mojave Desert, USA: an ecological legacy. Arid Land Res. Manag. 16 (3), 245–258. https://doi.org/10.1080/153249802760284793.

Berndt, D., Clifford, J., 1994. Using dynamic time warping to find patterns in time series. Workshop on Knowledge Discovery in Databases 398, 359–370. http://www.aaai.org/Papers/Workshops/1994/WS-94-03/WS94-03-031.pdf.

Bograd, S.J., Mendelssohn, R., Schwing, F.B., Miller, A.J., 2005. Spatial heterogeneity of sea surface temperature trends in the Gulf of Alaska. Atmosphere - Ocean 43 (3), 241–247. https://doi.org/10.3137/ao.430304.

Breiman, L., 2001. Random forests. Mach. Learn. 45 (1), 3–35. https://doi.org/10.1201/9780367816377-11.

Bruzzone, L., Prieto, D.F., 2000. Automatic analysis of the difference image for unsupervised change detection. IEEE Trans. Geosci. Remote Sens. 38 (3), 1171–1182. https://doi.org/10.1049/cp:20060496.

Bruzzone, L., Serpico, S.B., 1997. An iterative technique for the detection of land-cover transitions in multitemporal remote-sensing images. IEEE Trans. Geosci. Remote Sens. 35 (4), 858–867. https://doi.org/10.1109/36.602528.

Burrell, A.L., Evans, J.P., Liu, Y., 2017. Detecting dryland degradation using Time Series Segmentation and Residual Trend analysis (TSS-RESTREND). Remote Sens. Environ. 197, 43–57. https://doi.org/10.1016/j.rse.2017.05.018.

Chamizo, S., Stevens, A., Cantón, Y., Miralles, I., Domingo, F., Van Wesemael, B., 2012. Discriminating soil crust type, development stage and degree of disturbance in semiarid environments from their spectral characteristics. Eur. J. Soil Sci. 63 (1), 42–53. https://doi.org/10.1111/j.1365-2389.2011.01406.x.

Chapin, F.S., Kofinas, G.P., Folke, C., 2009. Principles of Ecosystem Stewardship: Resilience-Based Natural Resource Management in a Changing World (Springer Science & Business Media).

Chen, J., Ming, Y.Z., Wang, L., Shimazaki, H., Tamura, M., 2005. A new index for mapping lichen-dominated biological soil crusts in desert areas. Remote Sens. Environ. 96 (2), 165–175. https://doi.org/10.1016/j.rse.2005.02.011.

Chen, X., Wang, T., Liu, S., Peng, F., Tsunekawa, A., Kang, W., Guo, Z., & Feng, K. (2019). A new application of random forest algorithm to estimate coverage of moss-dominated biological. Remote Sens., 11(1286), 18.

Chen, X., Wang, T., Liu, S., Peng, F., Kang, W., Guo, Z., Feng, K., Liu, J., Tsunekawa, A., 2020. Spectral response assessment of moss-dominated biological soil crust coverage under dry and wet conditions. Remote Sens. 12 (7). https://doi.org/10.3390/rs12071158.

Dall'Olmo, G., Karnieli, A., 2002. Monitoring phenological cycles of desert ecosystems using NDVI and LST data derived from NOAA-AVHRR imagery. Int. J. Remote Sens. 23 (19), 4055–4071. https://doi.org/10.1080/01431160110115988.

Desgraupes, B., 2018. clusterCrit: clustering indices (R package version 1.2.8). https://cran.r-project.org/package=clusterCrit.

Diks, C., Panchenko, V., 2006. A new statistic and practical guidelines for nonparametric Granger causality testing. J. Econ. Dyn. Control. 30 (9–10), 1647–1669. https://doi.org/10.1016/j.jedc.2005.08.008.

Dunnington, D., 2020. ggspatial: spatial data framework for ggplot2 (R package version 1.1.3). https://cran.r-project.org/package=ggspatial.

Dutrieux, L.P., Verbesselt, J., Kooistra, L., Herold, M., 2015. Monitoring forest cover loss using multiple data streams, a case study of a tropical dry forest in Bolivia. ISPRS J. Photogramm. Remote Sens. 107, 112–125. https://doi.org/10.1016/j.isprsjprs.2015.03.015.

Eldridge, D.J., Leys, J.F., 2003. Exploring some relationships between biological soil crusts, soil aggregation and wind erosion. J. Arid Environ. 53 (4), 457–466. https://doi.org/10.1006/jare.2002.1068.

Evans, J., Geerken, R., 2004. Discrimination between climate and human-induced dryland degradation. J. Arid Environ. 57 (4), 535–554. https://doi.org/10.1016/S0140-1963(03)00121-6.

Fang, S., Yu, W., Qi, Y., 2015. Spectra and vegetation index variations in moss soil crust in different seasons, and in wet and dry conditions. Int. J. Appl. Earth Obs. Geoinf. 38, 261–266. https://doi.org/10.1016/j.jag.2015.01.018.

Granger, C.J.W., 1969. Investigating causal relations by econometric models and cross-spectral methods. Econometrica 37 (3), 424–438.

Hamed, K.H., Ramachandra Rao, A., 1998. A modified Mann-Kendall trend test for autocorrelated data. J. Hydrol. 204 (1–4), 182–196. https://doi.org/10.1016/S0022-1694(97)00125-X.

Hein, L., 2006. The impacts of grazing and rainfall variability on the dynamics of a Sahelian rangeland. J. Arid Environ. 64 (3), 488–504. https://doi.org/10.1016/j.jaridenv.2005.06.014.

Henao, J., Baanante, C., 2006. Agricultural Production and Soil Nutrient Mining in Africa: Implications for Resource Conservation and Policy Development. IFDC Tech. Bull, March.

Higginbottom, T.P., Symeonakis, E., 2014. Assessing land degradation and desertification using vegetation index data: current frameworks and future directions. Remote Sens. 6 (10), 9552–9575. https://doi.org/10.3390/rs6109552.

Hijmans, R. J. (2020). raster: geographic data analysis and modeling (R package version 3.0-12). https://cran.r-project.org/package=raster.

Hill, J., Magier, J., Mehl, W., 1995. Land degradation, soil erosion and desertification monitoring in Mediterranean ecosystems. Remote Sens. Reviews 12 (1–2), 107–130.

Hill, J., Udelhoven, T., Jarmer, T., Yair, A., 2008. Land Cover in the Nizzana Sandy Arid Ecosystem. Mapping Surface Properties With Multi-Spectral Remote Sensing Data. In Arid Dune Ecosystems, Springer, Berlin, Heidelberg.

Hoffmann, C., Funk, R., Wieland, R., Li, Y., Sommer, M., 2008. Effects of grazing and topography on dust flux and deposition in the Xilingele grassland, Inner Mongolia. J. Arid Environ. 72 (5), 792–807. https://doi.org/10.1016/j.jaridenv.2007.09.004.

Jat, M.K., Garg, P.K., Khare, D., 2008. Monitoring and modelling of urban sprawl using remote sensing and GIS techniques. Int. J. Appl. Earth Obs. Geoinf. 10 (1), 26–43. https://doi.org/10.1016/j.jag.2007.04.002.

Jing, W., Tian, D., 2018. An improved distributed storage and query for remote sensing data. Procedia Computer Science 129, 238–247. https://doi.org/10.1016/j.procs.2018.03.071.

Johnson, D.E., Moroney, J.D., Cliff, R., Merkel, M.W., Smallman, L., Spirtas, M., 2009. Preparing and Training for the Full Spectrum of Military Challenges: Insights From the Experiences of China, France, the United Kingdom, India, and Israel. RAND, National Defense Research Institute.

Karnieli, A., 1997. Development and implementation of spectral crust index over dune sands. Int. J. Remote Sens. 18 (6), 1207–1220. https://doi.org/10.1080/014311697218368.

Karnieli, A., Sarafis, V., 1996. Reflectance spectrometry of cyanobacteria within soil crusts - a diagnostic tool. Int. J. Remote Sens. 8, 1609–1615.

Karnieli, A., Tsoar, H., 1995. Spectral reflectance of biogenic crust developed on desert dune sand along the Israel-Egypt border. Int. J. Remote Sens. 16 (2), 369–374. https://doi.org/10.1080/01431169508954403.

Karnieli, A., Shachak, M., Tsoar, H., Zaady, E., Kaufman, Y., Danin, A., Porter, W., 1996. The effect of microphytes on the spectral reflectance of vegetation in semiarid regions. Remote Sens. Environ. 57 (2), 88–96. https://doi.org/10.1016/0034-4257(95)00209-X.

Karnieli, A., Gabai, A., Ichoku, C., Zaady, E., Shachak, M., 2002. Temporal dynamics of soil and vegetation spectral responses in a semi-arid environment. Int. J. Remote Sens. 23 (19), 4073–4087. https://doi.org/10.1080/01431160110116338.

Karnieli, A., Qin, Z., Wu, B., Panov, N., Yan, F., 2014. Spatio-temporal dynamics of land-use and land-cover in the Mu Us Sandy Land, China, using the change vector analysis technique. Remote Sens. 6 (10), 9316–9339. https://doi.org/10.3390/rs6109316.

Kaufman, L., Rousseeuw, P.J., 2009. Finding groups in data: an introduction to cluster analysis. In John Wiley & Sons 344.

Kendall, M.G., 1955. Rank Correlation Methods.

Kidron, G.J., 2016. Goat trampling affects plant establishment, runoff and sediment yields over crusted dunes. Hydrol. Process. 30 (13), 2237–2246. https://doi.org/10.1002/hyp.10794.

Kneip, A., Li, X., MacGibbon, K.B., Ramsay, J.O., 2000. Curve registration by local regression. The Canadian Journal of Statistics/La Revue Canadienne de Statistique 28 (1), 19. https://doi.org/10.2307/3315879.

Kosmas, C., Kairis, O., Karavitis, C., Ritsema, C., Salvati, L., Acikalin, S., Alcalá, M., Alfama, P., Atlhopheng, J., Barrera, J., Belgacem, A., Solé-Benet, A., Brito, J., Chaker, M., Chanda, R., Coelho, C., Darkoh, M., Diamantis, I., Ermolaeva, O., ... Ziogas, A., 2013. Evaluation and Selection of Indicators for Land Degradation and Desertification Monitoring: Methodological Approach. Environmental Management 54 (5), 951–970. https://doi.org/10.1007/s00267-013-0109-6.

Lal, R., 2009. Soil degradation as a reason for inadequate human nutrition. Food Secur. 1 (1), 45–57. https://doi.org/10.1007/s12571-009-0009-z.

Leutner, B., Ned, H., Jakob, S.-W., 2019. RStoolbox: tools for remote sensing data analysis (R package version 0.2.6). https://cran.r-project.org/package=RStoolbox.

Liaw, A., Wiener, M., 2002. Classification and regression by randomForest (pp. 18–22). R News 2(3). https://cran.r-project.org/doc/Rnews/.

Lilliefors, H.W., 1976. On the Kolmogorov-Smirnov test for normality with mean and variance unknown. J. Am. Stat. Assoc. 62, 399–402. https://doi.org/10.2307/2283970.

Maechler, M., Rousseeuw, P., Struyf, A., Huber, M., & Hornik, K. (2019). cluster: cluster analysis basics and extensions (R package version 2.1.0).

Mann, H.B., 1945. Nonparametric tests against trend author. Econometrica 13 (3), 245–259. https://doi.org/10.2307/1907187.

Müller-Hansen, F., Cardoso, M.F., Dalla-Nora, E.L., Donges, J.F., Heitzig, J., Kurths, J., Thonicke, K., 2017. A matrix clustering method to explore patterns of land-cover transitions in satellite-derived maps of the Brazilian Amazon. Nonlinear Process. Geophys. 24 (1), 113–123. https://doi.org/10.5194/npg-24-113-2017.

Ohana-Levi, N., Knipper, K.R., Kustas, W.P., Anderson, M.C., Netzer, Y., Gao, F., Alsina, M.M., Sanchez, L., Karnieli, A., 2020. Spatiotemporal dynamics of evapotranspiration in a vineyard based on thermal satellite remote sensing. Remote Sens. 12, 2436. https://doi.org/10.3390/rs12152436 .

Ohana-Levi, N., Paz-Kagan, T., Panov, N., Peeters, A., Tsoar, A., Karnieli, A., 2019. Time series analysis of vegetation-cover response to environmental factors and residential development in a dryland region. GIsci. Remote Sens. 56 (3), 362–387. https://doi.org/10.1080/15481603.2018.1519093.

Otterman, J., 1974. Baring high-albedo soils by overgrazing: a hypothesized desertification mechanism. Science 186 (4163), 531–533.

Pal, M., 2005. Random forest classifier for remote sensing classification. Int. J. Remote Sens. 26 (1), 217–222. https://doi.org/10.1080/01431160412331269698.
Panigada, C., Tagliabue, G., Zaady, E., Rozenstein, O., Garzonio, R., Di Mauro, B., De Amicis, M., Colombo, R., Cogliati, S., Miglietta, F., Rossini, M., 2019. A new approach for biocrust and vegetation monitoring in drylands using multi-temporal Sentinel-2 images. Prog. Phys. Geogr. 43 (4), 496–520. https://doi.org/10.1177/0309133319841903.
Paz-Kagan, T., Panov, N., Shachak, M., Zaady, E., Karnieli, A., 2014. Structural changes of desertified and managed shrubland landscapes in response to drought: spectral, spatial and temporal analyses. Remote Sens. 6 (9), 8134–8164. https://doi.org/10.3390/rs6098134.
Pebesma, E., 2020. stars: spatiotemporal arrays, raster and vector data cubes (R package version 0.4-1). https://cran.r-project.org/package=stars.
Peng, J., Ma, J., Liu, Q., Liu, Y., Hu, Y., Li, Y., Yue, Y., 2018. Spatial-temporal change of land surface temperature across 285 cities in China: an urban-rural contrast perspective. Sci. Total Environ. 635, 487–497. https://doi.org/10.1016/j.scitotenv.2018.04.105.
Permatasari, P.A., Fatikhunnada, A., Liyantono, Setiawan, Y., Syartinilia, Nurdiana, A., 2016. Analysis of agricultural land use changes in Jombang Regency, East Java, Indonesia using BFAST method. Procedia Environ. Sci. 33, 27–35. https://doi.org/10.1016/j.proenv.2016.03.053.
Petitjean, F., Inglada, J., Gancarski, P., 2012. Satellite image time series analysis under time warping. IEEE Trans. Geosci. Remote Sens. 50 (8), 3081–3095.
Pohlert, T., 2020. trend: non-parametric trend tests and change-point detection (R package version 1.1.2). https://cran.r-project.org/package=trend.
Prosser, C.W., Sedivec, K.K., Barker, W.T., 2000. Tracked vehicle effects on vegetation and soil characteristics. J. Range Manag. 53 (6), 666–670. https://doi.org/10.2307/4003164.
Puigdefábregas, J., 2005. The role of vegetation patterns in structuring runoff and sediment fluxes in drylands. Earth Surf. Process. Landf. 30 (2), 133–147. https://doi.org/10.1002/esp.1181.
Qin, Z., Karnieli, A., Berliner, P., 2001. A mono-window algorithm for retrieving land surface temperature from Landsat TM data and its application to the Israel-Egypt border region. Int. J. Remote Sens. 22 (18), 3719–3746. https://doi.org/10.1080/01431160010006971.
Qin, Z., Li, W., Burgheimer, J., Karnieli, A., 2006. Quantitative estimation of land cover structure in an arid region across the Israel-Egypt border using remote sensing data. J. Arid Environ. 66 (2), 336–352. https://doi.org/10.1016/j.jaridenv.2005.11.003.
R Core Team, 2020. R: A Language and Environment for Statistical Computing (R Foundation for Statistical Computing).
Ravi, S., Breshears, D.D., Huxman, T.E., D'Odorico, P., 2010. Land degradation in drylands: interactions among hydrologic-aeolian erosion and vegetation dynamics. Geomorphology 116 (3–4), 236–245. https://doi.org/10.1016/j.geomorph.2009.11.023.
Rawat, J.S., Kumar, M., 2015. Monitoring land use/cover change using remote sensing and GIS techniques: a case study of Hawalbagh block, district Almora, Uttarakhand, India. Egypt. J. Remote Sens. Space Sci. 18 (1), 77–84. https://doi.org/10.1016/j.ejrs.2015.02.002.
Reed, S.C., Maestre, F.T., Ochoa-Hueso, R., Kuske, C.R., Darrouzet-Nardi, A., Oliver, M., ... Belnap, J., 2016. Biocrusts in the context of global change. In Biological soil crusts: An organizing principle in drylandsSpringer, Cham.
Richter, R., Schlapfer, D., 2019. Atmospheric / Topographic Correction for Satellite Imagery. DLR - German Aerospace Center, Wessling, Germany.
Romani, L.A.S., Gonçalves, R.R.V., Amaral, B.F., Chino, D.Y.T., Zullo, J., Traina, C., Sousa, E.P.M., Traina, A.J.M., 2011. Clustering analysis applied to NDVI/NOAA multitemporal images to improve the monitoring process of sugarcane crops. 2011 6th International Workshop on the Analysis of Multi-Temporal Remote Sensing Images, Multi-Temp 2011 - Proceedings, pp. 33–36 https://doi.org/10.1109/Multi-Temp.2011.6005040.
Romesburg, C., 2004. Cluster Analysis for Researchers. Lulu.com.
Roskin, J., Porat, N., Tsoar, H., Blumberg, D.G., Zander, A.M., 2011. Age, origin and climatic controls on vegetated linear dunes in the northwestern Negev Desert (Israel). Quat. Sci. Rev. 30 (13–14), 1649–1674. https://doi.org/10.1016/j.quascirev.2011.03.010.
Roskin, J., Blumberg, D.G., Porat, N., Tsoar, H., Rozenstein, O., 2012. Do dune sands redden with age? The case of the northwestern Negev dunefield, Israel. Aeolian Res. 5, 63–75. https://doi.org/10.1016/j.aeolia.2011.11.004.
Rozenstein, O., Siegal, Z., Blumberg, D.G., Adamowski, J., 2016. Investigating the backscatter contrast anomaly in synthetic aperture radar (SAR) imagery of the dunes along the Israel–Egypt border. Int. J. Appl. Earth Obs. Geoinf. 46, 13–21. https://doi.org/10.1016/j.jag.2015.11.008.
Sarda-Espinosa, A., 2019. dtwclust: time series clustering along with optimizations for the dynamic time warping distance (R package version 5.5.6). https://cran.r-project.org/package=dtwclust.
Shmueli, D.F., Khamaisi, R., 2015. Resettlement planning 1948–present. Israel's Invisible Negev Bedouin. Springer, Cham https://doi.org/10.1007/978-3-319-16820-3_7.
Siegal, Z., Tsoar, H., & Karnieli, A. (2013). Effects of prolonged drought on the vegetation cover of sand dunes in the NW Negev Desert: field survey, remote sensing and conceptual modeling. Aeolian Res., 9, 161–173. doi:https://doi.org/10.1016/j.aeolia.2013.02.002.
Sivakumar, M.V.K., 2007. Interactions between climate and desertification. Agric. For. Meteorol. 142 (2–4), 143–155. https://doi.org/10.1016/j.agrformet.2006.03.025.
Smith, W.K., Dannenberg, M.P., Yan, D., Herrmann, S., Barnes, M.L., Barron-Gafford, G.A., Biederman, J.A., Ferrenberg, S., Fox, A.M., Hudson, A., Knowles, J.F., MacBean, N., Moore, D.J.P., Nagler, P.L., Reed, S.C., Rutherford, W.A., Scott, R.L., Wang, X., Yang, J., 2019. Remote sensing of dryland ecosystem structure and function: progress, challenges, and opportunities. Remote Sens. Environ. 233 (November 2018), 111401. https://doi.org/10.1016/j.rse.2019.111401.
Solangi, G.S., Siyal, A.A., Siyal, P., 2019. Spatiotemporal dynamics of land surface temperature and its impact on the vegetation. Civ. Eng. J. 5 (8), 1753–1763. https://doi.org/10.28991/cej-2019-03091368.
Solescu, D., 2020. Challenges faced by the Romanian land forces regarding training for the operations in the urban environment. Land Forces Academy Review 25 (2), 115–120. https://doi.org/10.2478/raft-2020-0014.
Stones, A.I., Treed, C., 2006. African soil exhaustion. Science 312 (5770). https://doi.org/10.1126/science.312.5770.31d 31d-31d.
Tsoar, H., Karnieli, A., 1996. What determines the spectral reflectance of the Negev-Sinai sand dunes? Int. J. Remote Sens. 17, 513–525. https://doi.org/10.16309/j.cnki.issn.1007-1776.2003.03.004.
Tsoar, H., Møller, J.T., 1986. The role of vegetation in the formation of linear sand dunes. In: Nickling, W.G. (Ed.), Aeolian Geomorphology. Allen and Unwin, Boston, pp. 75–95.
Vallet, E., 2016. Borders, Fences and Walls: State of Insecurity? Routledge
Verbesselt, J., Hyndman, R., Newnham, G., Culvenor, D., 2010. Detecting trend and seasonal changes in satellite image time series. Remote Sens. Environ. 114 (1), 106–115. https://doi.org/10.1016/j.rse.2009.08.014.
Viovy, N., 2000. Automatic classification of time series (acts): a new clustering method for remote sensing time series. Int. J. Remote Sens. 21 (6–7), 1537–1560. https://doi.org/10.1080/014311600210308.
Weber, B., Olehowski, C., Knerr, T., Hill, J., Deutschewitz, K., Wessels, D.C.J., Eitel, B., Büdel, B., 2008. A new approach for mapping of biological soil crusts in semidesert areas with hyperspectral imagery. Remote Sens. Environ. 112 (5), 2187–2201. https://doi.org/10.1016/j.rse.2007.09.014.
Weber, B., Büdel, B., Belnap, J., 2016. Biological Soil Crusts: An Organizing Principle in Drylands. 226th ed. (Ecological Studies).
Weng, Q., Lu, D., 2008. A sub-pixel analysis of urbanization effect on land surface temperature and its interplay with impervious surface and vegetation coverage in Indianapolis, United States. Int. J. Appl. Earth Obs. Geoinf. 10 (1), 68–83. https://doi.org/10.1016/j.jag.2007.05.002.
Wickham, H., 2016. ggplot2: Elegant Graphics for Data Analysis. Springer-Verlag New York. https://ggplot2.tidyverse.org.
Wilcox, B.P., 2010. Ecohydrology bearing - invited commentary transformation ecosystem change and ecohydrology: ushering in a new era for watershed management. Ecohydrology 130 (February), 126–130. https://doi.org/10.1002/eco.
Wilcox, B.P., Sorice, M.G., Young, M.H., 2011. Dryland ecohydrology in the anthropocene: taking stock of human-ecological interactions. Geogr. Compass 5 (3), 112–127. https://doi.org/10.1111/j.1749-8198.2011.00413.x.
Yair, A., 1990. Runoff generation in a sandy area—the nizzana sands, Western Negev, Israel. Earth Surf. Process. Landf. 15 (7), 597–609. https://doi.org/10.1002/esp.3290150703.
Yair, A., Almog, R., Veste, M., 2011. Differential hydrological response of biological topsoil crusts along a rainfall gradient in a sandy arid area: Northern Negev desert, Israel. Catena 87 (3), 326–333. https://doi.org/10.1016/j.catena.2011.06.015.
Yang, D., Kanae, S., Oki, T., Koike, T., Musiake, K., 2003. Global potential soil erosion with reference to land use and climate changes. Hydrol. Process. 17 (14), 2913–2928. https://doi.org/10.1002/hyp.1441.
Zaady, E., Katra, I., Yizhaq, H., Kinast, S., Ashkenazy, Y., 2014. Inferring the impact of rainfall gradient on biocrusts' developmental stage and thus on soil physical structures in sand dunes. Aeolian Res. 13, 81–89. https://doi.org/10.1016/j.aeolia.2014.04.002.
Zaady, E., Eldridge, D.J., Bowker, M.A., 2016. In: Weber, B., Büdel, B., Belnap, J. (Eds.), Biological Soil Crusts: An Organizing Principle in Drylands vol. 226. Springer, Cham.
Zanchetta, A., Bitelli, G., Karnieli, A., 2016. Monitoring desertification by remote sensing using the Tasselled Cap transform for long-term change detection. Nat. Hazards 83, 223–237. https://doi.org/10.1007/s11069-016-2342-9.
Zhang, S.Y., Liu, C., 2006. Predicting the lumber volume recovery of Picea mariana using parametric and non-parametric regression methods. Scand. J. For. Res. 21 (2), 158–166. https://doi.org/10.1080/02827580500531791.
Zhang, Y.M., Wang, H.L., Wang, X.Q., Yang, W.K., Zhang, D.Y., 2006. The microstructure of microbiotic crust and its influence on wind erosion for a sandy soil surface in the Gurbantunggut Desert of Northwestern China. Geoderma 132 (3–4), 441–449. https://doi.org/10.1016/j.geoderma.2005.06.008.
Zhang, X., Sun, R., Zhang, B., Tong, Q., 2008. Land cover classification of the North China Plain using MODIS_EVI time series. ISPRS J. Photogramm. Remote Sens. 63 (4), 476–484. https://doi.org/10.1016/j.isprsjprs.2008.02.005.
Zhang, Z., Tang, P., Huo, L., Zhou, Z., 2014. MODIS NDVI time series clustering under dynamic time warping. International Journal of Wavelets, Multiresolution and Information Processing 12 (05), 1461011. https://doi.org/10.1142/s0219691314610116.
Zhu, Z., 2017. Change detection using landsat time series: a review of frequencies, preprocessing, algorithms, and applications. ISPRS J. Photogramm. Remote Sens. 130, 370–384. https://doi.org/10.1016/j.isprsjprs.2017.06.013.
Zhu, X., Cai, F., Tian, J., Williams, T.K.A., 2018. Spatiotemporal fusion of multisource remote sensing data: literature survey, taxonomy, principles, applications, and future directions. Remote Sens. 10 (4). https://doi.org/10.3390/rs10040527.